

Far Ultraviolet Performance of the Berkeley Spectrograph During the ORFEUS-SPAS II Mission¹

Mark Hurwitz, Stuart Bowyer, Robert Bristol, W. Van Dyke Dixon, Jean Dupuis, Jerry Edelstein, Patrick Jelinsky, Timothy P. Sasseen², and Oswald Siegmund
 Space Sciences Laboratory, University of California,
 Berkeley, CA 94720-7450

ABSTRACT

The Berkeley spectrograph aboard the ORFEUS telescope made its second flight on the 14-day ORFEUS-SPAS II mission of the Space Shuttle *Columbia* in November/December 1996. Approximately half of the available observing time was dedicated to the Berkeley spectrograph, which was used by both Principal and Guest Investigators. The spectrograph's full bandpass is 390–1218 Å; here we discuss its in-flight performance at far-ultraviolet (FUV) wavelengths, where most of the observations were performed. The instrument's effective area peaks at $8.9 \pm 0.5 \text{ cm}^2$ near 1020 Å, and the mean spectral resolution is 95 km s^{-1} FWHM for point sources. Over most of the spectral range, the typical night-time background event rate in each spectral resolution element was about 0.003 s^{-1} . Simultaneous background observations of an adjacent blank field were provided through a secondary, off-axis aperture. The Berkeley spectrograph's unique combination of sensitivity and resolution provided valuable observations of approximately 105 distinct astronomical targets, ranging in distance from the earth's own moon to some of the brightest AGN.

Subject headings: Instrumentation: spectrographs

1. INTRODUCTION

The German spacecraft Astro-SPAS, a deployable platform designed to meet the technical performance demands of astronomical payloads and similar scientific instruments, comprised the primary payload aboard shuttle mission STS-80 (*Columbia*). On this, its third flight, the platform carried a trio of far-ultraviolet instruments: two independent spectrographs within the 1 meter diameter ORFEUS telescope (Grewing et al. 1991) and the IMAPS objective-grating spectrograph (Jenkins et al. 1996). All three had flown on the Astro-SPAS' 5-day maiden voyage in September of 1993, but improvements in instrument performance, and the critical need for additional observation time, motivated a reflight. A photograph of the payload is shown in Plate 1.

With few exceptions, targets suitable for ORFEUS were too faint for IMAPS, so no attempt was made to coalign these instruments closely. Within the ORFEUS telescope a flip mirror was employed to direct

¹ Based on the development and utilization of ORFEUS (Orbiting and Retrievable Far and Extreme Ultraviolet Spectrometers), a collaboration of the Institute for Astronomy and Astrophysics of the University of Tuebingen, the Space Astrophysics Group, University of California, Berkeley, and the Landessternwarte Heidelberg.

²currently with Department of Physics, University of California, Santa Barbara, CA 93106

the optical beam to one spectrograph or the other. Hence in general only one of the three instruments was operated at a time. The available observing time was shared equally between Guest Investigators selected by peer review and the Principal Investigator teams who had provided the instruments. Flight operations were directed from a control complex at the Kennedy Space Center.

The general design of the Berkeley spectrograph has been discussed previously (Hurwitz & Bowyer 1986, 1996). We changed the instrument between missions only by overcoating of two of the four diffraction gratings (including the far ultraviolet grating) with silicon carbide, introducing the multiple apertures discussed below, and modifying the detector electronics to improve the imaging at high count rates. We did not recoat the KBr photocathode on the microchannel plate detectors; the delay-line anode detector systems are discussed in Stock et al. (1993). In this work we report on the performance and calibration of the spectrograph during the ORFEUS-SPAS II mission and the instrumental effects of interest to Guest Investigators and other users of the extracted data products.

2. THE ASTRO-SPAS PLATFORM AND ORFEUS TELESCOPE

The Astro-SPAS was fabricated by Daimler-Benz Aerospace in Ottobrunn, Germany. An extremely reliable platform offering high scientific performance at comparatively low cost, it relies on nonrenewable resources such as cold gas thrusters, batteries, and on-board recorders for primary data storage. The spacecraft was deployed on 20 November, and recovered on 4 December, 1996.

When observing with the Berkeley spectrograph, the on-board recorders capture data at a rate of about 131 kbits s^{-1} . Each photon event processed by our electronics requires 24 bits of encoding: 8 bits of Y coordinate, 15 of X, and 1 for detector identification. With an allowance for ancillary data, the maximum recordable event rate corresponds to about 4400 spectral photons s^{-1} . A slower telemetry link (8 kbits s^{-1} for the scientific instruments) enables a subset of the data to be transmitted to ground via the shuttle except during comparatively short periods (minutes to, on occasion, hours) when prohibited by the orientation of the shuttle or the unavailability of TDRSS.

For fine pointing, the spacecraft's attitude control system (ACS) utilizes tracking signals from a star tracker mounted parallel to the ORFEUS telescope axis (hereafter Z axis). Under normal circumstances the ACS achieves an absolute pointing error less than about $5''$ and, during the ORFEUS-SPAS II mission, a jitter of about $\pm 2''$ peak-to-peak. The roll angle about the Z axis is determined automatically by the ACS, which orients the telescope door for use as a sun shade. If a guide star pattern is not recognized by the tracker upon arrival at a specified target, the ACS is forced to rely on gyroscopes, introducing an absolute pointing error that generally places targets outside the $26''$ diameter spectrograph entrance aperture. Outside the nominal 50° (half-angle) sun avoidance cone, lack of suitable guide stars caused the loss of one or two targets during the ORFEUS-II mission. Observations within this cone were possible only in fortuitous circumstances (the presence of unusually bright guide stars and/or occultation of the sun by the earth's limb).

The ORFEUS telescope systems performed well throughout the mission. The mechanisms of potential concern (main telescope door, spectrograph flip mirror, and diaphragm selection blade) operated nominally. There are three available diaphragm positions, each of which corresponds to a unique aperture or combination of apertures at the focal plane. Position 1 contains a single on-axis aperture $20''$ in diameter and was rarely employed for Berkeley observations. Position 2 contains a single on-axis aperture $10'$ in diameter, used during the initial star tracker/telescope coalignment and for some observations of diffuse

backgrounds and extended objects. Position 3, most commonly used with our spectrograph, contains three apertures. For most observations the target was placed in the on-axis, 26" diameter hole. A second clear hole, about 1.4 times larger in area and displaced by 2'.4, usually admitted only diffuse sky glow, although serendipitous spectroscopy of astrophysical sources was performed in some crowded fields. A third aperture, 120" in diameter, is displaced by 5'.0 and covered by a tin filter approximately 1500 Å thick. The tin filter is virtually opaque to far-ultraviolet radiation and was employed primarily for observation of the EUV spectrum of the bright B star ϵ CMa.

3. FLIGHT ACTIVITIES AND THERMAL EFFECTS

A modest anomaly early in the mission delayed the initiation of science observations by several hours. Although preflight knowledge of the coalignment between the telescope and the star tracker is specified within $\pm 5'$, the actual misalignment (30') greatly exceeded the radius of the largest aperture. This offset caused some consternation among all the science teams until it was identified and resolved by the Berkeley group, which achieved final on-orbit coalignment to within the few arcsecond level around 326/08:00 (Day of Year / HH:MM, GMT).

Unlike sounding rockets and long-duration missions, the time scale for thermal changes in the instrument structure is neither much longer nor much shorter than the mission length. By necessity, both ORFEUS spectrograph teams refined the coalignment several times during the first few days; we also carried out frequent observations of the bright symbiotic binary RR Tel to characterize the Berkeley spectrograph wavelength scale. Based on thermal models and data from the ORFEUS-I mission, the structure should have cooled to near-equilibrium conditions by day four or five.

Beginning about four days into the mission, the Astro-SPAS was twice required to assume a “minimum drag” configuration, in which the platform orientation was held fixed with respect to the instantaneous velocity vector. These orientations were specified by shuttle flight directors to ensure a safe separation between the three bodies that were co-orbiting at the time (ORFEUS-SPAS, the shuttle, and the Wake Shield Facility [a secondary deployed payload]). Observations were not possible during these periods, the first of which began around 329/04:00 and lasted for ~ 4 hours. The IMAPS instrument was active immediately after this period; Berkeley operations resumed at 329/13:00. No anomalies in the science instruments associated with the first minimum drag orientation have been noted. The second minimum drag session began around 329/20:00, lasting ~ 12 hours. The spacecraft orientation seems to have differed from the first period (there are multiple orientations in which a minimum cross-section is presented). Although the full effects were not recognized at the time, the second minimum drag period subjected the spacecraft to prolonged asymmetrical radiative thermal loads unlike those present during normal operations. Temperatures increased significantly. A large offset arose between the telescope and star tracker axes, causing the outright loss of some Echelle spectrograph targets when observations were first resumed and necessitating frequent refinement of the alignment matrix as structures cooled. Berkeley observations resumed around 330/20:00. Post-flight analysis has revealed changes in the wavelength scale associated with thermal excursions persisting for many hours after the end of the second minimum drag period.

Once thermal equilibrium was restored, operations for the remainder of the mission were fairly routine. Essentially all of the lost observing time was recovered in an extra day appended to the preplanned time line. The extra day was deeply appreciated by the science teams and guest investigators, as its approval required a careful balancing of science return and mission risk. A crew exit hatch had become stuck, making

it impossible (short of an emergency depressurization of the cabin) for the astronauts to assist manually if difficulties arose in the recovery of the platform. Fortunately, recovery around 338/10:00 was routine.

4. EFFECTIVE AREA AND BACKGROUNDS

In-flight observations of the hot DA white dwarf HZ 43 provide the most reliable flux calibration for the Berkeley spectrograph. To compute a synthetic spectrum for HZ 43 we have adopted $T_{\text{eff}} = 50,000$ K and $\log(g[\text{cm}^{-2}]) = 8.0$, corresponding to the values adopted by Bohlin et al. (1995) for the HST/FOS flux calibration. These values agree with those in the literature (e.g., Napiwotzki et al. 1993). We use the grid of LTE-blanketed pure hydrogen white dwarf synthetic spectra computed by Vennes (1992) and used in the modeling of the ORFEUS-I spectra of MCT 0455–2812 and G191–B2B (Vennes et al. 1996). We normalize the model by the visual magnitude of 12.914 (Bohlin et al. 1995). We take into account the H I interstellar opacity, adopting a column of $8.7 \times 10^{17} \text{ cm}^{-2}$ determined by Dupuis et al. (1995). Interstellar absorption is important in the core of the strong Lyman lines and near the convergence of the series. An effective area curve is derived by dividing the count rate spectrum of HZ 43 by the synthetic spectrum (after convolution with the instrumental resolution profile). The result is fit with a fifth-order Legendre polynomial to retain the overall shape of the curve while removing structure on small spatial scales.

Two early observations of HZ 43 were lost because of the alignment difficulties mentioned previously. We use the helium-rich white dwarf MCT 0501–2858 (observed at 326/12:20 and several times subsequently) as a transfer standard to define the effective area curve during the first observing period. The complete family of effective area curves is shown in Figure 1.

After 329/03:15, the effective area is smooth and, aside from a possible change at the longest wavelengths, temporally stable. Most science observations were performed during the stable period. At earlier times the instrument response exhibits temporal variability. The time-line presented in Table 1 is the simplest that is consistent with the available data and our understanding of the instrument.

Because the effective area at early times (primarily during Shifts 2 and 3) relies on our best understanding of a changing instrument response, the flux calibration for these observations carries an uncertainty that varies with wavelength and must be inferred from Figure 1. After stabilizing, the effective area peaks at about 8.9 cm^2 at 1020 \AA . Relative variations among curves during the stable period correspond to no more than about $\pm 4\%$. We have estimated flux errors associated with uncertainties in the atmospheric parameters of HZ 43 to be about 5% by perturbing T_{eff} by ± 2000 K and the gravity by ± 0.2 dex. We carried out a consistency check with G191B2B by applying our effective area curve and comparing with synthetic spectra. The agreement is only fair if we model the spectrum of G191B2B with a pure hydrogen composition and atmospheric parameters from the literature. Metals contaminate the spectrum of G191B2B (Vennes et al. 1996), and a better agreement can be obtained by lowering the assumed effective temperature. We will investigate these effects in more detail in a future paper using models including line blanketing by heavy elements. We note that flux calibration for the ORFEUS-I spectra relied on observations of G191B2B and a pure hydrogen photospheric model. Intercomparison of targets common to both missions indicates that ORFEUS-I far ultraviolet fluxes (final extraction of October 1995) are systematically high, and should be multiplied by 0.9.

When the spectral photon event rate approaches the capacity of the telemetry system, instrument deadtime effects become important. The detector electronics create “stimulation” events at the detector edges at a rate (approximately 2 s^{-1}) that can be measured during slews and other quiet periods. The

Table 1: Early Mission Time-Line

Time	Event(s)	Result
Before launch	MCPs adsorb gas, lose “scrub”	Drop in A_{eff} near 1170 Å
326/09:30	Begin Berkeley Shift 2	First successful science observations
326/12:20	MCT 0501 observed	1170 Å dip present
326/19:20	End Shift 2	Use MCT 0501 curve for all Shift 2 obs.
After 326/19:20, Before 327/06:20	Optical contamination, source unk. Some desorption of MCP gases?	Overall lowering of A_{eff}
327/06:20	Begin Shift 3	High count-rate target completes “scrub”
327/06:59	HZ 43 observed	1170 Å dip gone, overall A_{eff} lower
327/16:40	End Shift 3	Use first HZ 43 curve for all Shift 3
328/17:03	Begin Shift 4	
329/03:15	HZ 43 observed	A_{eff} back to high level, no dip, stable
329/03:53	End Shift 4	Use mean of Shift 4 and subsequent HZ 43 obs. for remainder of mission

observed rate of these events during on-target pointings enables us to estimate the deadtime for genuine spectral photons. Data buffering and the nonperiodic nature of the telemetry sampling system ensure that the throughput for both stimulation and actual photon events is identical.

At a given detector X (dispersion direction) coordinate, the FWHM of the spectrum averages 2 to 3 pixels in Y. Our extraction procedure sums the counts over a 9-pixel (best-fit center \pm 4 pixels) range, which usually encompasses $> 96\%$ of the dispersed photon events. One X-pixel corresponds to about 0.3 " of sky; one Y-pixel corresponds to about 10". The general background is scaled from two strips, each spanning 3 pixels in Y, immediately above and below the spectral region of the detector.

When the current flow parallel to the MCP surface cannot replenish the electrons being drained from the channel walls, the modal gain may sag. Gain sag is a function of local count rate caused by unusually bright emission-line or continuum targets. Gain sag must therefore be discussed independently from overall deadtime effects, which are a function of total count rate (including background). Gain sag is of greatest concern near the center of the band, where the astigmatism or spectral height is minimized.

In the Y-dimension, gain sag causes a loss of spatial resolution, with the result that some source events are not contained within the nominal 9 Y-pixel extraction window. (Spectral spill-over unrelated to gain sag may also occur if the source falls very near the edge of the entrance aperture.) The remedy is to study the background extractions for evidence of spectral spill-over, and to adjust the background subtraction procedure accordingly.

The delay-line system that calculates the photon X coordinates is generally robust against gain sag, but high local count rates can lead to wavelength-dependent variations in throughput. A very bright continuum source may suffer an uncorrected loss of throughput over broad regions where the astigmatism is small. In addition, very local variations in the modal gain or in the rate of electron replenishment can mimic spectral features when the modal gain is severely depressed. Several bright stars, substantially exceeding the recommended count rate limit, were observed to allow intercomparison of our spectrograph with the less

sensitive Echelle instrument. For one such star, with a flux of 1.5×10^{-10} ergs cm $^{-2}$ Å $^{-1}$ s $^{-1}$ at 1050 Å, gain sag creates a 33% loss in throughput from roughly 1040 to 1060 Å. Spectral artifacts are also present in this region. These effects will be studied in greater detail, but are of concern for only the brightest targets.

At wavelengths longward of 1017 Å, the background event rate summed over 9 pixels in Y and 0.33 Å in wavelength (e.g., one spectral resolution element) is about 0.0044 s $^{-1}$ during the day and 0.003 s $^{-1}$ at night. Most of the night-time background is attributable to the detector dark rate and cosmic rays; the day-time increase is probably associated with stray Lyman α radiation. At wavelengths below about 976 Å, the background is significantly higher. This region of the detector is exposed to a light leak qualitatively different from the general stray light affecting longer wavelengths. This “bright corner” of the detector was noted during the ORFEUS-I mission. Baffles added to the optical path were expected to attenuate the leak to negligible levels, but did not accomplish this goal. Our current hypothesis is that radiation reaches these corners of the detector via the spectrograph flip mirror in its retracted position. In the “bright corner,” the corresponding day and night rates are 0.091 and 0.012 s $^{-1}$. Their ratio corresponds roughly to the day/night ratio of diffuse Ly α .

The irregular footprint of the light leak creates a crossover region between about 976 and 1017 Å within which the background cannot simply be scaled from the strips above and below the spectrum. To estimate the background here, we assume that the shape of the background in the spectral region and in the adjacent strips differs only by a translation in the X coordinate, which we determine from detector images collected during slew periods. It is possible for this procedure to introduce artificial features within the overlap region. Artifacts of this type are not expected to be as narrow as unresolved spectral features, nor are they likely to exceed 10% of the background in amplitude. As such, they are of potential concern only for certain types of analysis of very faint targets. Over much of the overlap region the bright O I airglow complex near 989 Å contaminates the spectrum in any case.

Grating scatter within the plane of dispersion creates a false continuum that is not eliminated by subtraction of the general background. Grating scatter will be roughly constant in counts per unit wavelength. Its magnitude can be estimated from portions of the spectrum where broad absorption lines or ionization edges extinguish the astrophysical flux; in our investigations of early-type stellar and white dwarf spectra we have found that grating scatter contributes about 0.28% of the average flux across the FUV band. The rapid decline in photocathode sensitivity with increasing wavelength ensures that grating scatter will not greatly exceed this level even for sources whose spectra rise fairly steeply.

Diffuse emission lines of local (geocoronal and interplanetary) origin are superimposed on the source spectrum. A spectrum obtained through the off-axis aperture can be used to estimate the strength of these lines. Care must be taken, however, to account properly for the larger diameter of the off-axis aperture, which increases not only the total counts but the width of the point-spread function for diffuse emission. To estimate the counts in the on-axis spectrum, the corresponding counts in the off-axis spectrum must be divided by 1.4 ± 0.12 . The uncertainty in the scaling factor reflects small-scale nonuniformities in the detector and imposes a limit on the reliability of the subtraction that becomes important when the brightness of the diffuse emission greatly exceeds that of the astrophysical source. The off-axis spectrum for each science observation, on-axis spectra of blank fields, and an IDL software procedure are available to facilitate the subtraction of line profiles. Finally, it is evident that diffuse Lyman α affected the microchannel plate gain and hence the effective area (at the $\sim 10\%$ level) during the mission. The sensitivity loss will be time-dependent, and may affect the on- and off- axis spectra differently. There are few sources, however, bright enough to permit meaningful measurements of the astrophysical flux at the wavelength of the bright diffuse Lyman α line.

5. SPECTRAL RESOLUTION AND WAVELENGTH SCALE

To determine the instrument's monochromatic point spread function, we have fit the observed line profiles of features in the spectrum of the bright symbiotic binary RR Tel. The profiles are well characterized by Gaussian functions, with FWHMs generally increasing with the ionization potential of the species as found by Penston et al. (1983). Correcting for the intrinsic width of the lines (estimated from Penston et al.) we find a mean instrumental profile of about 95 km s^{-1} FWHM or about 0.33 \AA .

Pre-flight laboratory measurements yielded a spectral resolution that is higher than the in-flight value by a factor of about 1.5. During the ORFEUS-SPAS I mission operational and scheduling difficulties had interfered with focusing activities, leading us to attribute the resolution loss to an uncorrected defocus. Early in the second mission we successfully observed RR Tel at a range of grating focus positions, but the line widths did not sharpen as much as expected. The detector imaging performance appears nominal; the aforementioned stimulation events are as narrow on orbit as in the laboratory. The spacecraft jitter, well characterized by the star tracker and, during the first mission, by the Berkeley Fine Guidance detector, makes a negligible contribution. It may be that some aspect of our laboratory setup – most probably a slight underillumination of the grating pupil – led to an overestimate of the system performance.

The fairly wide scatter in the measured FWHMs and the somewhat uncertain contribution of the intrinsic widths make it difficult to assess the potential for systematic variations of the instrumental profile with wavelength. Based on preflight measurements, it is likely that the FWHM is more constant in $\Delta\lambda$ than in velocity. Locally, the instrumental FWHM for any given feature can be affected (at the $\sim 10\%$ level) by small-scale distortions introduced by the microchannel plate fabrication process.

The relationship between the observed wavelength and detector X coordinate is straightforward over most of the bandpass. Optical raytracing and in-flight measurements of emission lines in RR Tel (longward of 950 \AA) and the Lyman absorption series in the white dwarfs (below 950 \AA) confirm that over most of the spectral range the wavelength is a linear function of X plus a smooth departure that does not exceed $\pm 0.13 \text{ \AA}$. Near the edges of the detector the image becomes compressed, leading to a steepening of the λ vs. X relationship. At the short-wavelength end, the converging Lyman absorption line series in the white dwarfs provides reference features at closely spaced wavelengths (Hurwitz & Bowyer 1995; note that in the ORFEUS-SPAS I mission the Lyman convergence was well separated from the edge of the detector). There is no corresponding reference pattern at the long wavelength edge of the detector, but longward of Lyman α the spectrum becomes unreliable in any case because of a reflection near that detector edge.

Temporal changes in the wavelength scale include both an offset and a linear “stretch.” We use a combination of diffuse emission lines and the repeated observations of RR Tel to characterize these effects.

The wavelength assigned by the current version of our spectral extraction software (as of 9 September 1997) reflects all the effects mentioned here, including the anomalous thermal conditions following the second minimum drag orientation. Relative wavelength errors within a given spectrum should be less than 0.1 \AA between 915 and 1216 \AA . However, because of the unknown placement of each target within the aperture, an overall offset of $\pm 0.5 \text{ \AA}$ may exist in any individual spectrum.

To establish a wavelength scale for the off-axis aperture, we apply a fixed offset, determined for an average of the strongest diffuse emission features, to the on-axis wavelength solution. Because the detectable diffuse emission features are widely spaced in wavelength, residual uncertainties (potentially at the 0.1 \AA level) do not create real ambiguity in their wavelength identification.

6. DETECTOR FLAT-FIELD EFFECTS

Prior to delivery of the instrument we characterized the detector's response to flux that is uniform (at least on small spatial scales) by directing a bright beam produced by an Argon gas discharge at a bead-blasted metal surface near the diffraction gratings. The beam flux is dominated by a handful of strong emission lines in the FUV bandpass. We collected 159,000 seconds of data with the far-ultraviolet detector operating at a moderate count rate (2000 to 4000 s⁻¹).

The flat-field illumination strikes the detector at approximately the same mean angle as does the genuine spectrum, but the spectrum is the convergence of a fast f/5 beam, whereas the flat-field illumination diverges from a small spot about 1 meter from the detector. The laboratory flat-field was collected under thermal conditions different from those on orbit. The detector response may be affected by the total or local count rate, mechanical shifts caused by launch (or landing) loads, or the simple passage of time. The laboratory flat-field is therefore useful for characterizing the distribution of fluctuations in the detector response, but not for detailed division of flight spectra.

In flight observations, detector artifacts may affect the dispersed astrophysical flux, the background that is present within the spectral extraction window (the contributing background), or the background that is measured outside the extraction window (the subtracted background). To estimate the magnitude of the first effect, we extracted a “spectrum” from the preflight flat-field image using the best-fit Y centroids derived from the flight data, weighting the counts in adjoining Y pixels in a fashion that closely approximates the distribution of events in actual flight spectra. To estimate the second effect, we performed a similar extraction, adopting uniform weighting over the full 9 Y-pixel spectral window.

From the resulting extractions we can determine the distribution of detector artifacts appropriate for a given spectral wavelength interval. We first bin the extractions at a given $\Delta\lambda$, then calculate the RMS dispersion of the excursions about an extraction that has been smoothed by 7 $\Delta\lambda$. The size of the smoothing interval is somewhat arbitrary. A broader smoothing would be more conservative, but unrealistic for most applications. In fitting an absorption line, for example, one would normally interpolate a continuum based on nearby adjacent spectral resolution elements. We show the results in Figure 2, where we have expressed the RMS or 1σ width of the distribution as a fraction of the measured signal. Shot noise contributes negligibly to these results and has been subtracted in quadrature. The upper tracing (solid line) is applicable to dispersed spectral counts; the lower tracing (dashed line) is applicable to contributing background counts. Below about 0.15 Å the curves fall precipitously because the finite detector resolution smoothes out such small-scale fluctuations. At the nominal instrument resolution of 0.33 Å, the RMS is about 6.4% and 5.5% of signal for the spectral and contributing background events, respectively. Binned at broader wavelength intervals, the dispersion of detector artifacts falls fairly rapidly. Even at 3 Å, however, RMS fluctuations exist at the level of 3 to 3.5% of signal. These fluctuations probably result from the microchannel plate boule structure; each boule spans about 3 Å of spectrum.

Artifacts in the *subtracted* background are generally negligible. In the Y dimension, such artifacts are automatically smoothed by 6 pixels (uniform weighting). Because the background varies only slowly in the X dimension, it can generally be smoothed fairly broadly in wavelength. For most applications we recommend smoothing the subtracted background by a boxcar with a full width of 1.2 Å. Smoothing over a broader interval can introduce difficulties near the crossover region where the background varies comparatively rapidly with wavelength, but may be helpful elsewhere. In the extracted spectral file, we pre-smooth the background by a uniform boxcar with a comparatively narrow width (0.19 Å). This retains effectively 100% of the system spectral resolution, which is important if a portion of the source spectrum

has spilled over into the background region. It is straightforward for the user to introduce the additional recommended background smoothing; the IDL procedure we provide to read the spectrum smoothes the background spectrum automatically.

7. SUMMARY / FUTURE PLANS

The Berkeley spectrograph aboard the ORFEUS telescope offers a unique and important combination of spectral resolution and effective area in the comparatively unexplored far-ultraviolet wavelength band. During the ORFEUS-SPAS II mission in November/December 1996, Principal and Guest Investigators utilized the spectrograph to observe some 105 astronomical targets. These data will enter the public domain in early to mid 1998.

Lyman/FUSE is not far from launch, and will offer a much higher spectral resolution and sensitivity for point sources. However, near-trivial modifications would enable the Berkeley spectrograph to achieve a significantly superior performance for studies of extended emission. New replicas of the current gratings and SiC overcoating of the primary mirror would allow the spectrograph to achieve 2 Å slit-limited resolution through a $45 \times 420''$ slit and an effective area of $\sim 50 \text{ cm}^2$ across the $900 - 1200 \text{ \AA}$ band. The angular resolution along the slit length would be better than $1'$. Such an instrument would be highly desirable for studies of intracluster gas, galaxies and their halos, supernova remnants, and other extended objects. At time of writing, there are no specific plans for a third flight of the payload.

We thank the NASA and DARA personnel whose efforts made the ORFEUS-SPAS II mission successful, especially the talented and patient crew of STS-80. Konrad Moritz and the Astro-SPAS operations team provided a marvelous spacecraft and a high level of support throughout the mission. Our fellow scientists at Tuebingen and Heidelberg and partners at Kayser-Threde GmbH made the ORFEUS program a scientific success and a personal pleasure. We thank Stephane Vennes for providing a grid of white dwarf model spectra that helped to determine the effective area curve, and offer special thanks to Brian Espey of the Johns Hopkins University for his generous assistance with the wavelength calibration. We acknowledge the support of NASA grant NAG5-696.

REFERENCES

Bohlin, R.C., Colina, L., & Finley, D.S. 1995, AJ, 119, 1316.

Dupuis, J., Vennes, S., Bowyer, S., Pradhan, A., and Thejll, P. 1995, ApJ, 455, 574.

Grewing, M. et al. 1991, in *Extreme Ultraviolet Astronomy*, ed. R.F. Malina and S. Bowyer, Elmsford: Pergamon, p. 437.

Hurwitz, M. and Bowyer, S. 1986, Proc. SPIE, 627, 375.

Hurwitz, M. and Bowyer, S. 1996, in *Astrophysics in the Extreme Ultraviolet*, ed. S. Bowyer and R.F. Malina, Dordrecht: Kluwer, p. 601.

Jenkins, E. B., Reale, M. A., Zucchino, P. M. and Sofia, U. J. 1996, Ap. Space Sci. 239, 315-360.

Napiwotzki, R., Barstow, M.A., Fleming, T., Holweger, H. Jordan, S., & Werner, K. 1993, AA, 278, 478.

Penston, M.V., et al. 1983, MNRAS 202, 833.

Stock, J., Siegmund, O.H.W., Hurwitz, M., Raffanti, R., Bowyer, S., and Lampton, M. 1993, Proc. SPIE 2006, 128.

Vennes, S. 1992, ApJ, 390, 590

Vennes, S., Chayer, P., Hurwitz, M., and Bowyer, S. 1996, Ap. J. 468, 898.

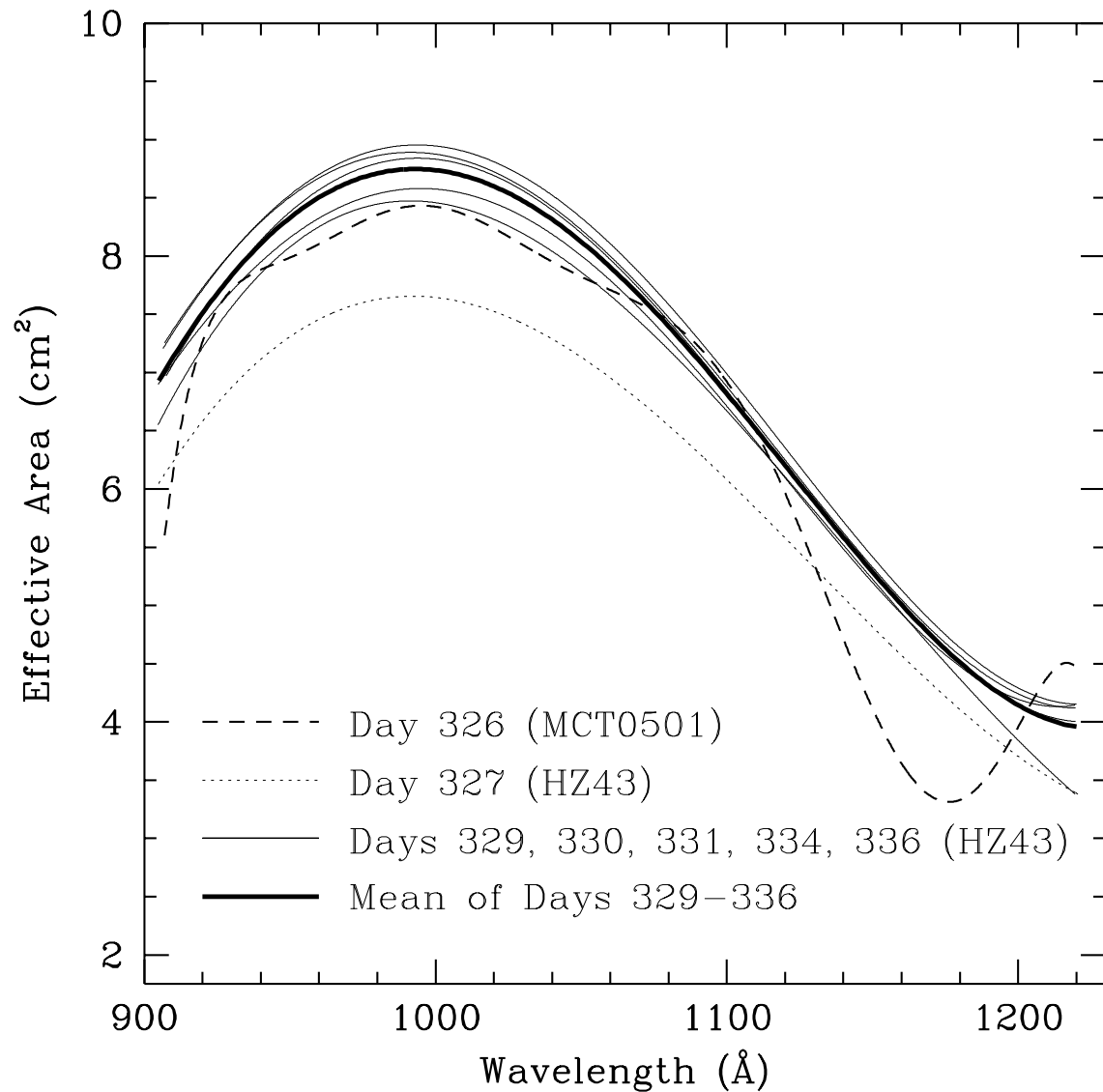


Fig. 1.— Far ultraviolet effective area curve for Berkeley spectrograph during ORFEUS-SPAS II mission.

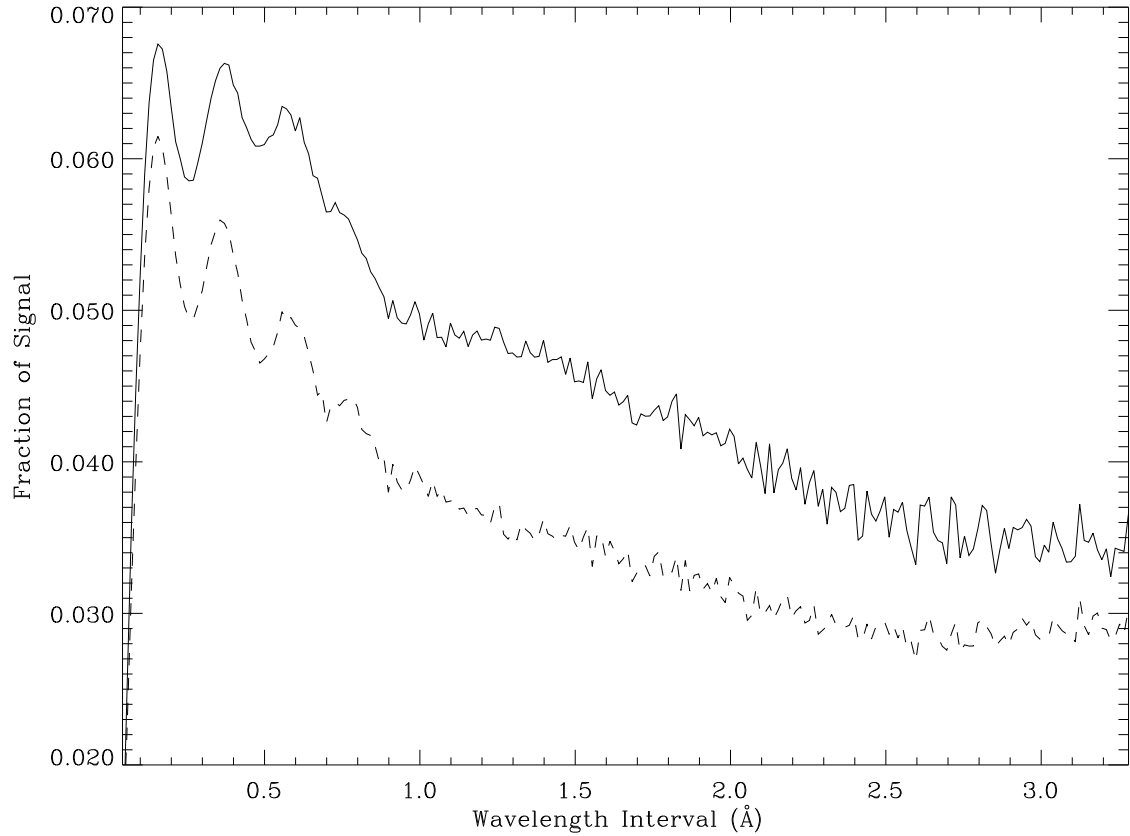


Fig. 2.— RMS dispersion of detector artifacts expressed as a fraction of the measured signal vs. wavelength interval. These data are based on preflight illumination that is uniform on small spatial scales. The solid line applies to dispersed spectral photon events; the dashed line applies to the contributing background events. The rapid fall at small wavelength intervals results from the finite detector resolution. At large wavelength intervals, the function declines because the increasing microchannel plate surface area leads to a smoother response.